INTERNATIONAL JOURNAL FOR NUMERICAL METHODS IN FLUIDS
Int. J. Numer. Meth. Fluids 2003; **42**:1155–1188 (DOI: 10.1002/fld.516)

A high-order finite difference method for incompressible fluid turbulence simulations

Eric Vedy[†], Stephane Viazzo[‡] and Roland Schiestel[*,§]

Institut de Recherche sur les Phénomènes Hors Equilibre, I.R.P.H.E., U.M.R. 6594 CNRS/Universités d'Aix-Marseille I & II, 49, rue Frédéric Joliot Curie, B.P. 146, 13384 Marseille Cedex 13, France

SUMMARY

A Hermitian–Fourier numerical method for solving the Navier–Stokes equations with one non-homogeneous direction had been presented by Schiestel and Viazzo (*Internat. J. Comput. Fluids* 1995; **24**(6):739). In the present paper, an extension of the method is devised for solving problems with two non-homogeneous directions. This extension is indeed not trivial since new algorithms will be necessary, in particular for pressure calculation. The method uses Hermitian finite differences in the non-periodic directions whereas Fourier pseudo-spectral developments are used in the remaining periodic direction. Pressure–velocity coupling is solved by a simplified Poisson equation for the pressure correction using direct method of solution that preserves Hermitian accuracy for pressure. The turbulent flow after a backward facing step has been used as a test case to show the capabilities of the method. The applications in view are mainly concerning the numerical simulation of turbulent and transitional flows. Copyright © 2003 John Wiley & Sons, Ltd.

KEY WORDS: Navier–Stokes equations; Hermitian methods; large eddy simulation; turbulence; boundary layer; backward facing step flow

1. INTRODUCTION

We present a numerical method for solving the three-dimensional unsteady Navier–Stokes equations written in primitive variables for an incompressible fluid, devised for applications to large eddy simulations of turbulent flows. The basic concepts were originally developed by Schiestel and Viazzo [1] and applied to compute flows involving two directions with periodic boundary conditions and a third one with non-periodic boundary conditions. The new extension proposed here enables to deal with more complex situations and especially flows involving two non-homogeneous directions, thus enlarging the field of applications. Indeed,

---

[*] Correspondence to: R. Schiestel IRPHE (UMR 6594), CNRS/Universités d'Aix-Marseille I et II, 49 Rue Frédéric Joliot Curie, B.P. 146, 13384 Marseille Cedex 13, France.

[†] Present address: TNO TPD, Sound and Vibration Division, Stieltjesweg 1, P.O. Box 155, 2600 A D Delft, The Netherlands.

[‡] Present address: Ecole des Mines de Nantes, La Chantrerie, 4, rue A. Kastler, B.P. 20722, F44307 Nantes Cedex 3, France.

[§] E-mail: schieste@irphe.univ-mrs.fr

Received April 2000
Revised 6 January 2003

most applications of practical interest imply at least two non-homogeneous directions. This is the case for instance for numerous developing flows that are two-dimensional in the mean such as jets and boundary layer flows. This extension developed in the present work is not just an outgrowth of the Schiestel and Viazzo [1] method, but it embodies several important new aspects corresponding to a different computer code.

Hermitian methods and compact schemes, first introduced by Krause [2] and Hirsch [3] have been applied to fluid flow problems by several authors [4–7]. They produce high accuracy finite difference schemes that in practice can almost compete with spectral methods [8]. Recently, compact differencing approximations have been applied to DNS and LES. In particular, applications of such methods for simulation of turbulence are reported by Kral and Zang [9], Guo and Adams [10] and Schiestel and Viazzo [1].

In the first part, we give a detailed description of the numerical method. The space discretization makes use of a staggered grid and the derivatives are evaluated using fourth-order Hermitian relations in the two inhomogeneous directions and Fourier polynomial expansions in the third one which is homogeneous. The time advancement is based on an iterative splitting scheme. The Hermitian Poisson equation for pressure is replaced by its finite difference analogue and is solved using a diagonalization technique. This is one of the main new ingredients of the method proposed here. Thanks to the secondary internal iterative process, the fourth-order accuracy of the numerical scheme is recovered for pressure and velocities. Thus, the numerical method guaranties good conservation properties and high accuracy that are required for meaningful large eddy simulations.

The second part is devoted to validation test cases. We first verify the accuracy of the proposed method by means of comparisons between analytical and numerical solutions of the Navier–Stokes equations. The method is then applied to the computation of two-dimensional laminar flow over a backward facing step for Reynolds numbers ranging from $Re = 50$ up to 500 and the results are compared with experimental and numerical results.

In the last part of this paper, in order to demonstrate the efficiency of the method for numerical simulation of turbulence, we present two different applications to turbulent backward facing step flows using Large Eddy Simulation. The method is applied to the filtered Navier–Stokes equations, and the subgrid scales are modelled with a Smagorinsky eddy viscosity model. The first simulation is a fully turbulent flow in a channel with a sudden expansion at $Re = 27\,600$. In a second simulation we also consider the turbulent flow in an open channel with a small step at $Re = 13\,800$.

2. NUMERICAL METHOD

2.1. Navier–Stokes equations

We consider the flow of an incompressible newtonian fluid with density ρ and viscosity ν in a fixed reference frame $(Oxyz)$. The fluid domain, $\Omega \subset \mathbb{R}^3$, is infinite and periodic along the spanwise direction (Oy), while in the two other directions (x and z) the domain is bounded by the surface $\partial\Omega$.

Using U_{ref} and L_{ref} to denote velocity and length scales, the velocities are normalized by U_{ref} and the pressure is normalized by ρU_{ref}^2. The dimensionless equations of motion written in primitive variables (velocity $\mathbf{U} = (u, v, w)$ and pressure p) are the well-known Navier–Stokes equations:

$$\frac{\partial \mathbf{U}}{\partial t} = -\mathbf{U}\cdot\nabla\mathbf{U} - \nabla p + \frac{1}{Re}\Delta\mathbf{U} \tag{1}$$

together with the continuity equation:

$$\nabla\cdot\mathbf{U} = 0 \tag{2}$$

where the parameter Re is the Reynolds number defined by $Re = U_{\text{ref}}L_{\text{ref}}/\nu$.

In the spanwise direction, the flow is considered as homogeneous, hence periodic boundary conditions can be used. In the two inhomogeneous directions, the velocity components are usually set to specified values, depending on the problem under consideration: zero (no-slip condition) on the solid boundaries, and any other value, assumed to be known, for inflow and outflow boundaries. At the exit boundary, however, different types of boundary conditions can be used depending on the particular application, such as given pressure and zero transverse components of velocity. If all the velocity components are given, they must satisfy the compatibility condition:

$$\int_{\partial\Omega} (\mathbf{U}\cdot\mathbf{n})\,\mathrm{d}S = 0 \tag{3}$$

where **n** is the unit normal vector on the boundary. If the pressure is fixed together with the v and w-velocity components, then the longitudinal u-component can be recovered from continuity (2). In the present method, the Navier–Stokes equations will be written in the skew-symmetric form recommended by Zang [11]:

$$\frac{\partial \mathbf{U}}{\partial t} = -\frac{1}{2}\mathbf{U}\cdot\nabla\mathbf{U} - \frac{1}{2}\nabla(\mathbf{U}\cdot\mathbf{U}) - \nabla p + \frac{1}{Re}\Delta\mathbf{U} \tag{4}$$

along with the continuity equation (2). Indeed, the skew-symmetric form proved to possess nice conservation properties, even on shifted grids [12, 1]

2.2. *Space discretization*

The computational domain (Figure 1) is a rectangular box extending from $x = 0$ to L_x in the main flow direction (Ox), $y = 0$–L_y in the spanwise direction (Oy) and from $z = 0$ to L_z in the vertical direction (Oz). The numbers of discretization points are, respectively, N_x, N_y and N_z in the x, y and z directions and ΔX, ΔY, ΔZ stand for the corresponding grid spacings.

The space discretization makes use of a staggered mesh (a MAC type mesh) which prevents pressure checkerboarding to occur. It also avoids the need of complex appropriate boundary conditions for pressure [4]: velocity components u, v, w are, respectively, located at nodes $((i+\frac{1}{2})\Delta X,\ j\Delta Y,\ k\Delta Z)$, $(i\Delta X,\ (j+\frac{1}{2})\Delta Y,\ k\Delta Z)$ and $(i\Delta X,\ j\Delta Y, (k+\frac{1}{2})\Delta Z)$ while pressure nodes are located at $(i\Delta X, j\Delta Y, k\Delta Z)$, see Figures 2 and 3. Then the staggered velocities will be denoted $\mathbf{U} = (u_{i+\frac{1}{2},j,k}, v_{i,j+\frac{1}{2},k}, w_{i,j,k+\frac{1}{2}})$, whereas the pressure remains located at nodes $p = p_{i,j,k}$.

In the two inhomogeneous directions first- and second-order derivatives are given by Hermitian relations (fourth-order accurate) recalled in Appendix A. Hermitian relations for first-order derivatives lead to tridiagonal systems that are solved using the Thomas algorithm. Hermitian relations for second-order derivatives are explicit.

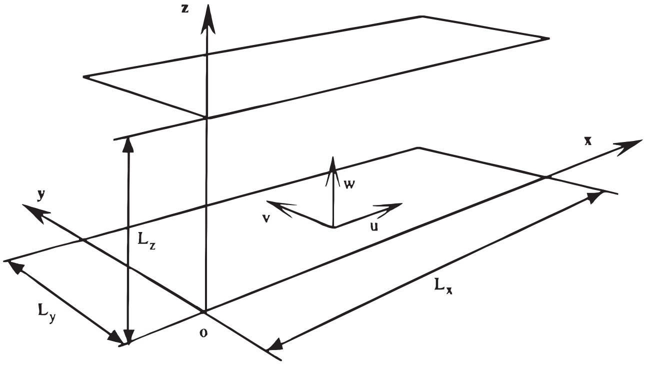

Figure 1. Sketch of the fluid flow domain.

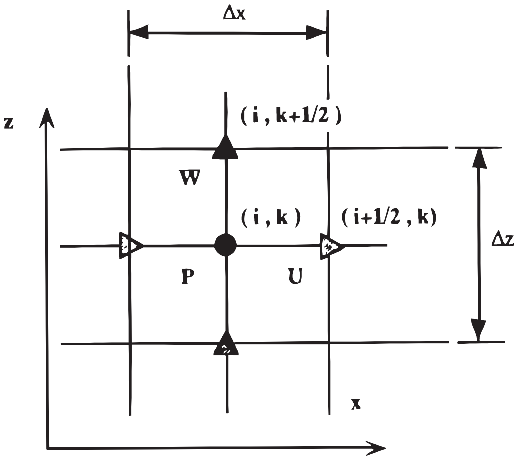

Figure 2. Staggered arrangement for interior grid points of the mesh.

We also introduce a variable change to allow local mesh refinements. If ξ denotes the X or Z co-ordinate on a regular transformed mesh, while ζ denotes the x or z physical co-ordinate, the $\zeta=\zeta(\xi)$ function is supposed to be defined analytically (see Appendix C).

Derivatives are then evaluated in the transformed co-ordinate system (X,Z) and true derivatives with respect to (x,z) are obtained by

$$\frac{\partial f}{\partial \zeta}=g_{\xi}\frac{\partial f}{\partial \xi} \quad \text{and} \quad \frac{\partial^2 f}{\partial \zeta^2}=g_{\xi}^2\frac{\partial^2 f}{\partial \xi^2}+h_{\xi}\frac{\partial f}{\partial \xi} \tag{5}$$

with

$$g_x=\frac{\mathrm{d}\xi}{\mathrm{d}\zeta} \quad \text{and} \quad h_{\xi}=\frac{\mathrm{d}^2\xi}{\mathrm{d}\zeta^2}$$

These changes do not lead to strong local truncation errors as long as the step variation is smooth [13].

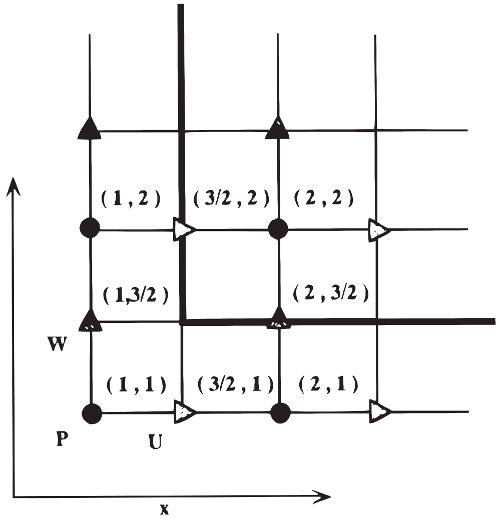

Figure 3. Arrangement of grid points at the boundaries in the (x,z) plane.

In the spanwise direction, interpolations, first- and second-order derivatives are based on Fourier polynomial expansions. The method is developed in physical space using pseudo-spectral formalism.

2.3. *Time advancement*

The time integration is based on a second-order accurate Adams-Bashforth/Crank–Nicolson time scheme. Only the $\delta^2_{\zeta\zeta} f$ type contributions (see Equation (A7)) in the diffusion terms are included in the Crank–Nicolson scheme and thus treated implicitly. All the remaining terms, except the pressure term which is considered separately, are included in the Adam–Bashforth part of the scheme denoted by **H**. The **H** term includes in particular the convective terms, the first-order derivatives stemming from variable changes, the terms γ_ξ in Equation (A7), together with the second derivatives in the y direction:

$$\mathbf{H} = \tfrac{1}{2}(\nabla\mathbf{U}\cdot\mathbf{U} + \mathbf{U}\cdot\nabla\mathbf{U}) + \mathbf{A}$$

where **A** denotes the diffusive terms that are not included in the Crank–Nicolson part.

The discrete momentum equations are then

$$\frac{1}{\Delta t}(\mathbf{U}^{n+1} - \mathbf{U}^n) = \Xi^{n,n-1} - \mathbf{G}p^{n+1} + \frac{1}{2Re}L(\mathbf{U}^{n+1} + \mathbf{U}^n) \tag{6}$$

with

$$D\cdot\mathbf{U}^{n+1} = 0 \tag{7}$$

where **G** denotes the approximation of the gradient operator, D the approximation of the divergence operator (Hermitian approximation in x and z and Fourier approximation in y) and L is the discrete second-order Laplacian in the (x,z) plane. The superscripts n and $n+1$

are referring to values at times $n\Delta t$ and $(n+1)\Delta t$. The system that has to be solved at each time step is now rewritten in the form

$$\frac{1}{\Delta t}(\mathbf{U}^{n+1}-\mathbf{U}^{n}) = -\frac{1}{2}(3\mathbf{H}^{n}-\mathbf{H}^{n-1}) - \mathbf{G}p^{n+1} + \frac{1}{2Re}(g_X^2\delta_{XX}^2 + g_Z^2\delta_{ZZ}^2)(\mathbf{U}^{n+1}+\mathbf{U}^{n}) \tag{8}$$

These momentum equations are solved on the velocity nodes and the divergence free constraint is enforced at pressure nodes.

2.4. Solution technique

2.4.1. Splitting scheme. The solution of the former system makes use of a fractional step technique [1] which consists in splitting the time advancement in two steps. In the first step, an approximation of the velocity field is computed which is not divergence-free because it does not satisfy the incompressibility constraint:

$$\frac{1}{\Delta t}(\hat{\mathbf{U}}-\mathbf{U}^{n}) = \mathbf{H}^{n,n-1} - \mathbf{G}p^{n} + \frac{1}{2Re}L(\hat{\mathbf{U}}+\mathbf{U}^{n}) \tag{9}$$

in the second step the velocity vector is corrected by an additive gradient term in order to recover Equation (6):

$$\frac{1}{\Delta t}(\mathbf{U}^{n+1}-\hat{\mathbf{U}}) = -\mathbf{G}\Phi \tag{10}$$

Taking the divergence of Equation (10) and setting $D\cdot\mathbf{U}^{n+1}=0$, gives the Poisson equation for Φ:

$$D\cdot\mathbf{G\Phi} = \frac{1}{\Delta t}D\cdot\hat{\mathbf{U}} \tag{11}$$

Then, from Equations (9) and (10), by comparison with Equation (6) the pressure is updated:

$$p^{n+1} = p^{n} + \mathbf{\Phi} + \frac{\Delta t}{2Re}L\mathbf{\Phi}$$

In fact, due to the rather complicated expression of the $D\cdot\mathbf{G}$ operator, the procedure described above has been modified to proceed by internal iterations. The time advancement is thus achieved through an iterative fractional step technique [1]. At the internal iteration m, an approximation $\mathbf{U}^{n+1,m}$ of $\mathbf{U}^{n+1}$ is deduced from the momentum equation using the values of pressure and velocities at the previous internal iteration:

$$\frac{1}{\Delta t}(\mathbf{U}^{n+1,m}-\mathbf{U}^{n}) = \Xi^{n,n-1} - \mathbf{G}p^{n+1,m-1} + \frac{1}{2Re}L(\mathbf{U}^{n+1,m-1}+\mathbf{U}^{n}) \tag{12}$$

In a second step the velocity field is corrected by

$$\mathbf{U}^{n+1,m+1} = \mathbf{U}^{n+1,m} - \Delta t\mathbf{G}\Phi \tag{13}$$

and finally the pressure field at the new internal iteration $m+1$ is obtained by

$$p^{n+1,m+1} = p^{n+1,m} + \Phi \tag{14}$$

The correction Φ is solution of the Poisson equation:

$$D \cdot \mathbf{G}\Phi = \frac{1}{\Delta t} D \cdot \mathbf{U}^{n+1,m} \tag{15}$$

The major difference from Equation (11) is that when the internal iteration process is converged the solution of (15) is always $\Phi = 0$. So, it is now permissible to replace the Hermitian approximation of the Laplacian in the left-hand side by the central difference approximation which is much simpler. After one internal iteration the new velocity field is still not divergence free and others internal iterations are required to get better approximation of $\mathbf{U}$. These operations are repeated until the divergence of the velocity field becomes less than a specified value. From a practical point of view, the convergence criterion for this internal iteration procedure is considered to be reached when the relative residuals verify:

$$\max\left[\frac{D \cdot \mathbf{U}^{n+1,m}}{\mathbf{U}_{\max}^{n+1,m}}, \frac{|\mathbf{U}^{n+1,m+1} - \mathbf{U}^{n+1,m}|}{\mathbf{U}_{\max}^{n+1,m}}\right] \leqslant \varepsilon \tag{16}$$

The parameter ε which characterizes the precision of the computation is chosen equal to 10^{-6} for all the applications considered in the following:

For the first internal iteration, at each time step, we take

$$\mathbf{U}^{n+1,0} = \mathbf{U}^{n}, \quad P^{n+1,0} = P^{n} \tag{17}$$

When the convergence is reached, at the internal iteration M, we have

$$D \cdot \mathbf{U}^{n+1,M} = 0, \quad \Phi = 0$$

and

$$\mathbf{U}^{n+1} = \mathbf{U}^{n+1,M}, \quad P^{n+1} = P^{n+1,M}$$

The discrete Poisson equation for pressure, obtained from the two derivatives on staggered grid nodes reads:

$$\begin{aligned}&\frac{g_{X,i}}{\Delta X^2}\{g_{X,i-1+\frac{1}{2}}\Phi_{i-1,j,k} - (g_{X,i-1+\frac{1}{2}} + g_{X,i+\frac{1}{2}})\Phi_{i,j,k} + g_{X,i+\frac{1}{2}}\Phi_{i+1,j,k}\}\\&\quad + \frac{g_{Z,k}}{\Delta Z^2}\{g_{Z,k-1+\frac{1}{2}}\Phi_{i,j,k-1} - (g_{Z,k-1+\frac{1}{2}} + g_{Z,k+\frac{1}{2}})\Phi_{i,j,k} + g_{Z,k+\frac{1}{2}}\Phi_{i,j,k+1}\}\\&\quad + d_Y^2\Phi_{i,j,k} = \frac{1}{\Delta t} D \cdot \mathbf{U}_{i,j,k}^{n+1,m}\end{aligned} \tag{18}$$

where d_y^2 is the approximation of second-order derivative in the spanwise direction.

We write it in a more convenient way

$$(\delta_{xx}^2 + \delta_{zz}^2 + d_y^2)\Phi = \frac{1}{\Delta t} D \cdot \mathbf{U}^{n+1,m} \tag{19}$$

This procedure preserves the overall fourth-order accuracy of the numerical scheme although the Poisson equation for pressure correction is only second-order accurate. Indeed, the velocity divergence in the right-hand side of (19) is still an Hermitian discretization.

2.4.2. Compatibility condition. Assuming that the velocity components are given on the boundaries, the corresponding conditions for the pressure correction are homogeneous Neumann conditions. Writing $\partial\Omega$ for the bounding surface of the computational domain Ω and $\mathbf{n}$ for the normal unit vector to $\partial\Omega$, this condition reads

$$\left.\frac{\partial\mathbf{\Phi}}{\partial\mathbf{n}}\right|_{\partial\Omega}=0 \tag{20}$$

However, they must be written as central differences:

$$\Phi_{1,k}=\Phi_{2,k},\quad \Phi_{Nx,k}=\Phi_{Nx-1,k},\quad \Phi_{i,1}=\Phi_{i,2},\quad \Phi_{i,Nz}=\Phi_{i,Nz-1}$$

Integration of Equation (19) leads to the velocity compatibility condition:

$$\frac{1}{\Delta t}\int_{\partial\Omega}\mathbf{U}\cdot\mathbf{n}=\int_{\partial\Omega}\mathbf{G\Phi}\cdot\mathbf{n}=0 \tag{21}$$

reflecting the overall mass conservation on the domain. To ensure this property in the discrete sense, some minor adjustments in the discrete Laplacian are necessary (see Appendix B). Considering the previous remarks, these adjustments do not destroy the fourth-order accuracy of the method.

2.4.3. Diagonalization technique. Equation (19) has been solved using direct method. The benefit of direct methods over iterative methods of solution is decisive in particular with respect to computational time. This is a major addition made in the present extension of the method already presented in Reference [1]. This direct approach proved to be very interesting because of its several practical advantages. First of all, memory requirements are very limited, due to the fact that the technique only involves two-dimensional arrays. Also, the operators can be calculated in the preamble stage of the computer code, out of the main loops, saving lot of time. Taking the Fourier transform *TF*, of Equation (19) gives the following set of Helmholtz equations:

$$(\delta_{xx}^2+\delta_{zz}^2-k_y^2)TF_y(\mathbf{\Phi})=TF_y\left(\frac{1}{\Delta t}D\cdot\mathbf{U}^{n+1,m}\right) \tag{22}$$

For each wave number k_y we write it in the following matrix form:

$$\mathbf{D}_{xx}^2\mathbf{\Phi}+\mathbf{\Phi}\mathbf{D}_{zz}^{2^{\mathrm{T}}}-k_y^2\mathbf{\Phi}=\mathbf{S} \tag{23}$$

where $\mathbf{\Phi}$ is a $(\mathrm{N}_x-2)\times(\mathrm{N}_z-2)$ matrix of unknowns $\Phi_{i,k}(i=2,Nx-1,k=2,Nz-1)$, $\mathbf{D}_{xx}^2$ and $\mathbf{D}_{zz}^2$ are tridiagonal matrices of dimensions $(N_x-2)\times(N_x-2)$ and $(N_z-2)\times(N_z-2)$ including the boundary conditions.

This equation is solved using a diagonalization technique [14–16] which expresses $\mathbf{D}_{xx}^2$ and $\mathbf{D}_{zz}^2$ in terms of products:

$$\mathbf{D}_{xx}^2=\mathbf{P}_x\mathbf{\Lambda}_x\mathbf{P}_x^{-1}\quad\text{and}\quad\mathbf{D}_{zz}^2=\mathbf{P}_z\mathbf{\Lambda}_z\mathbf{P}_z^{-1}$$

where $\mathbf{\Lambda}_x = \mathrm{diag}(\lambda_{x,1}, \lambda_{x,2}, \dots, \lambda_{x,N_X-2})$ and $\Lambda_Z = \mathrm{diag}(\lambda_{z,1}, \lambda_{z,2}, \dots, \lambda_{z,N_Z-2})$ are diagonal matrices composed of the eigenvalues of $\mathbf{D}^2_{xx}$ and $\mathbf{D}^2_{zz}$. The matrices $\mathbf{P}_x$ and $\mathbf{P}_z$ are built on their corresponding eigenvectors. Both matrices $\mathbf{D}^2_{xx}$ and $\mathbf{D}^2_{zz}$ are diagonalizable for they can be written as the products of a diagonal and a tridiagonal symmetric (hence diagonalizable) matrix [17].

Writing $\tilde{\mathbf{\Phi}} = \mathbf{P}_x^{-1}\mathbf{\Phi}$ and $\tilde{\mathbf{S}} = \mathbf{P}_x^{-1}\mathbf{S}$, Equation (23) gives $\mathbf{\Lambda}_x\tilde{\mathbf{\Phi}} + \tilde{\mathbf{\Phi}} D^{2^{\mathrm{T}}}_{zz} - k_y^2\tilde{\mathbf{\Phi}} = \tilde{\mathbf{S}}$ Again setting $\breve{\mathbf{\Phi}} = \tilde{\mathbf{\Phi}}\mathbf{P}_z^{-1^{\mathrm{T}}}$ and $\breve{\mathbf{S}} = \tilde{\mathbf{S}}\mathbf{P}_z^{-1^{\mathrm{T}}}$, it turns that $\Lambda_x\breve{\mathbf{\Phi}} + \breve{\mathbf{\Phi}}\Lambda_z - k_y^2\breve{\mathbf{\Phi}} = \breve{\mathbf{S}}$ which yields:

$$\breve{\mathbf{\Phi}}_{i,k} = \frac{\breve{\mathbf{S}}_{i,k}}{\lambda_{x_i} + \lambda_{z_k} - k_y^2} \tag{24}$$

The values of $\mathbf{\Phi}$ are finally deduced from the relation $\Phi = P_x\tilde{\Phi} = P_x\bar{\tilde{\Phi}}P_z^{\mathrm{T}}$.

When Neumann boundary conditions are used for Φ, both $\mathbf{D}^2_{xx}$ and $\mathbf{D}^2_{zz}$ matrices are singular (they have a zero eigenvalue $\lambda_{x,i_0} = 0$ and $\lambda_{z,k_0} = 0$). In the particular case where $k_y = 0$, this singularity prevents to get the solution of Equation (22). In fact, there is an infinite number of solutions, because the pressure field is defined within an additive constant. The method retained here, which is a consequence of the velocity compatibility condition, consists in setting $\breve{\Phi}_{i_0,k_0} = 0$, if $\breve{S}_{i_0,k_0} = 0$. Since $\mathbf{D}^2_{xx}$ and $\mathbf{D}^2_{zz}$ are only space dependent, the calculation of their eigenvalues and eigenvectors is needed once for all, before starting the whole iteration process. At each time step, the solution of the Poisson equation will be reduced to four matrix products for each wave number.

An interesting alternative of this diagonalization method would be to solve Equation (15) keeping fourth-order discretization in the left-hand side. Heavier calculation results from this practice, but secondary iterations can be avoided (see, Reference [16]).

3. NUMERICAL TESTS OF THE NAVIER–STOKES SOLVER

3.1. Preliminary tests of the Poisson equation solution

The method of solution of the Poisson equation for the pressure correction is checked by comparison of the numerical solution with an exact analytical solution in two dimensions.

First a Neumann problem is defined by

$$\Delta\mathbf{\Phi} = \mathbf{S} \quad \text{in } \mathbf{\Omega} = \{-1 \leqslant x \leqslant 1, -1 \leqslant z \leqslant 1\}$$

with the boundary conditions: $\partial\mathbf{\Phi}/\partial x(\pm 1, z) = 0$ and $\partial\mathbf{\Phi}/\partial z(x, \pm 1) = 0$.

A second problem of mixed type is defined by

$$\Delta\mathbf{\Phi} = S \quad \text{in } \mathbf{\Omega} = \{-1 \leqslant x \leqslant 1, -1 \leqslant z \leqslant 1\}$$

with the boundary conditions: $\partial\mathbf{\Phi}/\partial x(+1, z) = 0$, $\partial\mathbf{\Phi}/\partial z(x, \pm 1) = 0$ and $\mathbf{\Phi}(-1, z) = 1/2\pi^3[\frac{1}{2}\cos(2\pi z) + 2\cos(\pi z)]$.

In both cases the right-hand side of the equation is given by

$$S(x,z) = \frac{1}{2\pi}\cos(\pi x)\left[\frac{5}{2}\cos(2\pi z) + 4\cos(\pi z)\right]$$

and an analytical solution for the two previous problems is given by the function:

$$\mathbf{\Phi}_{\text{analyt}}(x,z) = -\frac{1}{2\pi^3}\cos(\pi x)\left[\frac{1}{2}\cos(2\pi z) + 2\cos(\pi z)\right]$$

In order to verify the validity of the method, the maximal errors and the mean errors of the numerical solution in comparison with the analytical solution are calculated on the inner nodes.

$$\text{Mean quadradic error:}\quad \left(\frac{1}{(N_x-2)(N_z-2)}\sum_{i=2,k=2}^{N_x-1,N_z-1}(\phi-\phi_a)^2_{i,k}\right)^{1/2}$$

$$\text{Maximum error:}\quad \max_{\substack{i=2,N_x-1\\ k=2,N_z-1}} |(\phi-\phi_a)_{i,k}|$$

The tests are made for several different meshes with the same number of discretization points in the two directions x and z, for uniform meshes and for non-uniform meshes. These results presented in Figures 4(a) and 4(b) versus the space step $h = \Delta X = \Delta Z$ show that the errors thus obtained are of the order $\mathbf{O}(\mathrm{h}^2)$ in every case. It is also verified that when Neumann boundary conditions are used, the numerical solution is indeed the solution whose mean value is zero.

3.2. Test of the Navier–Stokes solver against a two-dimensional steady analytical solution

In order to check the accuracy of the numerical scheme, we compare the numerical results $\mathbf{U} = (u,w)$ and p to the analytical values $\mathbf{U}_a = (u_a, w_a)$ and p_a. Their dimensionless expressions, based upon $U_{\text{ref}} = U_{\max}$, $U_{\max}$ being the maximum velocity in the inflow plane and $L_{\text{ref}} = L_z/2$, the half-width of the channel, are given by

$$u_a = (1-z^2)(1-z\mathrm{e}^{-x}),\ w_a = \frac{1}{4}(1-z^2)^2\mathrm{e}^{-x} \quad \text{and} \quad p_a = -\frac{2x}{Re} \tag{25}$$

which are the solutions of the NS equations in which an adequate forcing term $\mathbf{F} = (f_x, f_z)$ is added. The forcing term can be easily deduced analytically from the knowledge of velocity components and pressure (Equation (25)):

$$\begin{aligned} f_x &= \frac{1}{4}(1-z^2)^2\mathrm{e}^{-x}[2z - z^2\mathrm{e}^{-x} - \mathrm{e}^{-x}] - \frac{1}{Re}[-z(1-z^2)\mathrm{e}^{-x} - 2 + 6z\mathrm{e}^{-x}] - \frac{2}{Re} \\ f_z &= -\frac{1}{4}(1-z^2)^3\mathrm{e}^{-x} - \frac{1}{Re}\left[\frac{1}{4}(1-z^2)^2 + 3z^2 - 1\right]z\mathrm{e}^{-x} \end{aligned} \tag{26}$$

The considered equation is thus

$$\frac{\partial \mathbf{U}}{\partial t} = -\mathbf{U}\cdot\nabla\mathbf{U} - \nabla p + \frac{1}{Re}\Delta\mathbf{U} + \mathbf{F} \tag{27}$$

The computational domain is $L_z = 2$ high and $L_x = 10$ long (in dimensionless quantities). The following boundary conditions are set at the inflow section: $u = u_a$, $w = w_a$ with the condition for ϕ: $\partial\phi/\partial x = 0$. No-slip boundary conditions for both u and w, are used at the walls: $u = 0, w = 0$ and the corresponding condition for ϕ is again $\partial\phi/\partial z = 0$. For the outflow section,

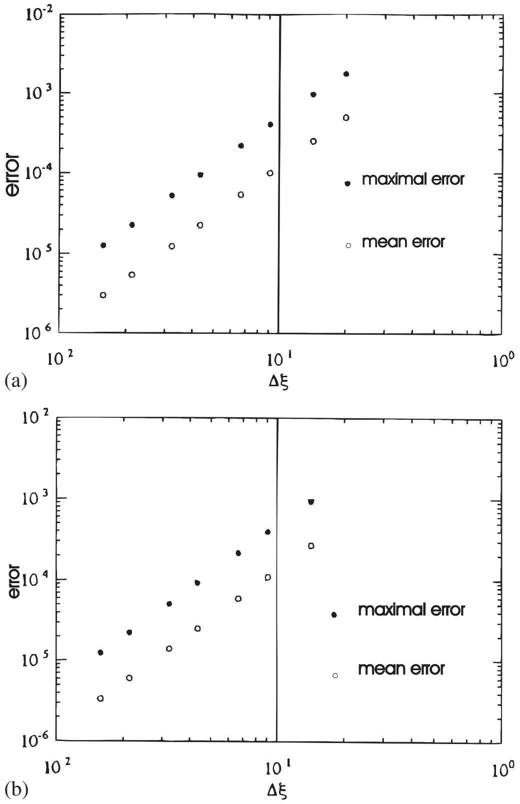

Figure 4. Influence of grid size on the accuracy of the numerical solution of the Poisson equation using centred differences. (a) Mixed boundary conditions and (b) Neumann boundary conditions.

we set $\partial w/\partial x = 0$ and $p = 0$, u being extrapolated to fulfil the continuity equation and ϕ is equal to zero. For this, the continuity equation $g_x \partial u/\partial X + g_z \partial w/\partial Z = 0$ is written at the node $(Nx - 1, k)$ taking into account the Hermitian relations for derivatives on staggered mesh:

$$u_{Nx-1+\frac{1}{2},k} = \Delta x \left[-23 \frac{g_{z(k),k}}{g_{x(i),Nx-1}} \left(\frac{\partial w}{\partial Z} \right)_{Nx-1,k} + \left(\frac{\partial u}{\partial X} \right)_{Nx,k} \right] + 26 u_{Nx-2+\frac{1}{2},k} - u_{Nx-3+\frac{1}{2},k} \tag{28}$$

The initial conditions are given by

$$u = u_a(x = 0) = (1 - z^2)(1 - z)$$
$$w = w_a(x = 0) = \tfrac{1}{4}(1 - z^2)^2 \quad \text{and} \quad p = 0$$

The grids are tightened in the two directions x and z, the stretching parameters being $a_X = 0.9$ and $a_Z = 0.9$ and then the space step is varied in order to determine the precision of the numerical scheme. The comparisons are carried out for several mesh sizes, using the same variable changes (refinement near the inflow plane and near the walls) in each case and the

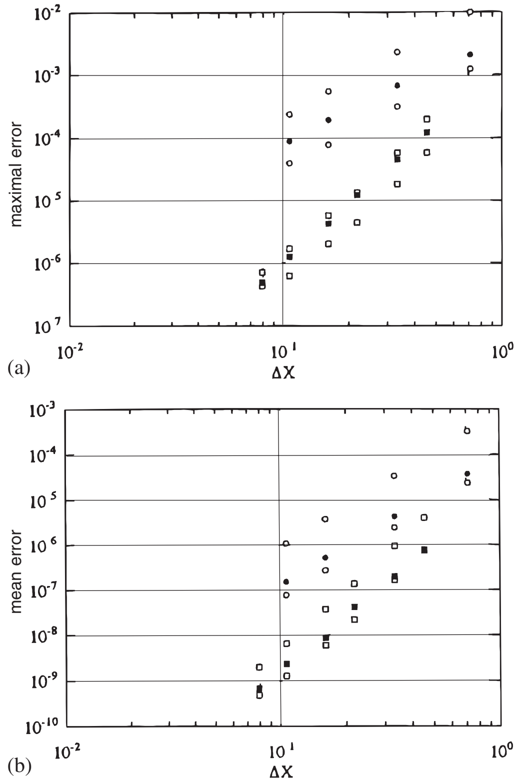

Figure 5. Influence of grid size on the precision of the numerical solution of the two-dimensional Navier–Stokes equations on variable mesh. (a) Square mean values of errors and (b) maximum of errors. Centred second-order differences: ○ (u), ⊙ (w), ● (p); Hermitian fourth-order scheme: □ (u), ⊡ (w), ■ (p).

same number of grid points in both directions x and z. For each variable, we compute the mean and maximum errors (at the interior grid points) of the numerical solution relatively to the analytical solution:

$$\text{The mean quadratic error } Q(u) = \left(\frac{1}{(N_x-2)(N_z-2)} \sum_{i=2,k=2}^{N_x-1,N_z-1} (u-u_a)_{i,k}^2 \right)^{\frac{1}{2}} \tag{29}$$

$$\text{The maximum error } M(u) = \max_{\substack{i=2,N_z-1\\ k=2,N_z-1}} |(u-u_a)_{i,k}| \tag{30}$$

The results are reported in Figures 5 and 6 (maximum errors and mean quadratic errors) and are also compared to the values obtained with a centred difference scheme (second-order accurate).

The results in Figure 5(a) present the mean quadratic errors for u, w and p versus the space step Δx: the measured slopes are, respectively, 4.4, 4.4 and 4.1. Figure 5(b) presents the maximum errors and the slopes are, respectively, 3.3, 3.1 and 3.2. These figures show that

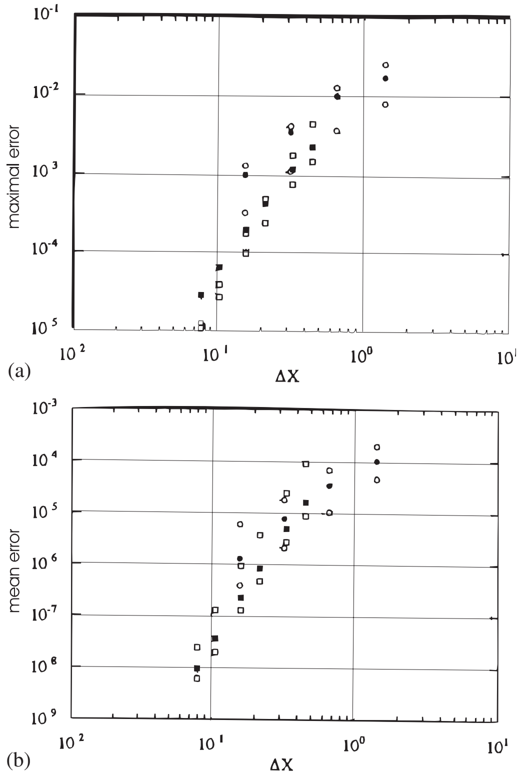

Figure 6. Influence of grid size on the precision of the numerical solution of the two-dimensional Navier–Stokes equations on uniform mesh. (a) Square mean values of errors and (b) maximum of errors (symbols: see Figure 5).

the whole scheme is indeed fourth-order accurate and that hermitian relations are much better than second-order centred differences. The loss of accuracy araising on the maximum errors, which are always located at the boundaries, can be explained by the third-order approximation of the boundary relations.

Some results are presented in Figure 6 for a uniform mesh. The slopes of the mean quadratic errors for u, w and p are, respectively, 4.7, 4.2 and 4.3, whereas the maximum errors are, respectively, 3.4, 2.8 and 2.5. So, the variable mesh does not damage significantly the accuracy of the numerical scheme. In practice, less than 10 internal iterations are necessary to reach a 10^{-14} maximum error on the velocity divergence.

Figure 7 displays the streamwise and vertical velocity components at various locations (using variable mesh with $N_x = N_z = 96$).

3.3. Laminar flow over a backward facing step

We consider the two-dimensional flow in a channel with a sudden expansion (Figure 8). Velocity and length scales of reference are, respectively, the bulk velocity in the inflow section

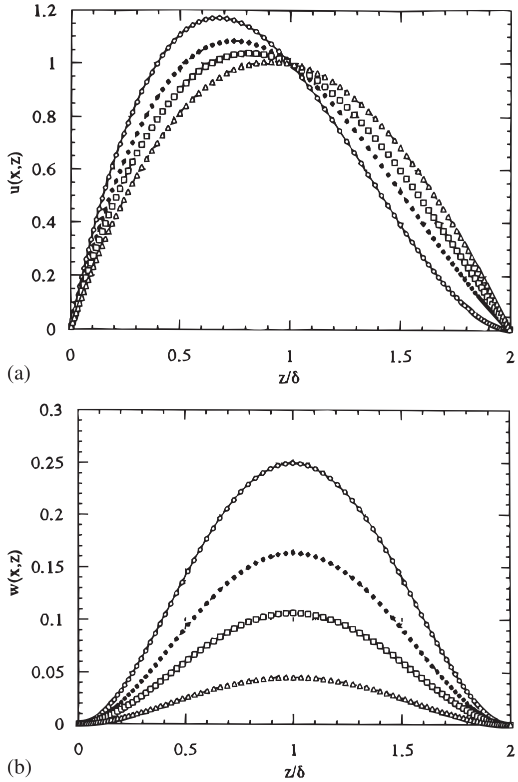

Figure 7. Comparison between numerical solution and analytical solution of the two-dimensional Navier–Stokes equations on a 96×96 mesh using Hermitian schemes. (a) u-velocity component and (b) w-velocity component. Lines: analytical solution, Symbols: numerical solution (— — ——, ◇: $x/h=0.0$; - - - - -, ♦: $x/h=0.43$; - - - -, □: $x/h=0.84$; - - - Δ: $x/h=1.71$).

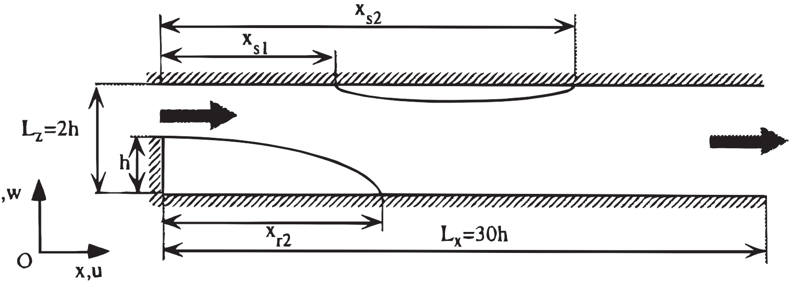

Figure 8. Sketch of the backward facing step flow in a channel.

U_{bulk} and the step height h. The channel length is $L_x = 30$ h and its height is $L_z = 2$ h.

This flow has been chosen as a typical reference case for testing the proposed method, considering that several experimental and numerical data are available in the scientific literature.

Table I. Bidimensional flow past a backward facing step.

Case No.	Re_h	Initial condit.	$N_x \times N_z$	Scheme	Exit b.c.	x_{r_2}/h	x_{s_1}/h	x_{s_2}/h
1	50	Channel	48 × 32	H	N	3.3	—	—
2	100	1	48 × 32	H	N	5.4	—	—
3	150	2	48 × 32	H	N	7.1	—	—
4	200	3	64 × 48	H	N	8.6	8.1	9.1
5	250	4	64 × 48	H	N	9.4	8.3	13.1
6	300	5	96 × 72	H	N	10.5	8.6	16.0
7	350	6	96 × 72	H	N	11.5	8.9	19.0
8	400	7	96 × 72	H	N	12.2	9.5	21.5
9	450	8	128 × 96	H	N	12.9	10.	23.5
10	500	9	128 × 96	H	N	13.5	10.8	25.5
11	50	Channel	48 × 32	C	N	3.1	—	—
12	100	11	48 × 32	C	N	5.2	—	—
13	150	12	48 × 32	C	N	7.1	—	—
14	200	13	64 × 48	C	N	8.8	—	—
15	250	14	64 × 48	C	N	9.9	6.1	13.1
16	300	15	96 × 72	C	N	10.1	7.4	18.2
17	350	16	96 × 72	C	N	11.6	8.3	21.8
18	400	17	96 × 72	C	N	12.3	8.4	25.5
19	450	8	128×96	H	C	12.5	9.5	22.2
20	500	9	128×96	H	C	13.2	10.0	26.4

Note: Scheme: H, fourth-order Hermitian; C, second-order centred and
Exit b.c.: N, zero gradient; C,convective condition.

The inflow boundary conditions are:

$$u = 6z(1-z) \quad \text{for } 0 \leqslant z \leqslant +1$$

$$u = 0 \quad \text{for } -1 \leqslant z \leqslant 0$$

and

$$w = 0 \quad \text{for } -1 \leqslant z \leqslant +1$$

The corresponding condition for the pressure correction is $\partial\phi/\partial x = 0$. For the outflow section we put: $\partial w/\partial x = 0$ and $p = 0$, the streamwise velocity component being extrapolated in order to fulfil the continuity equation. A no-slip boundary condition is used at the walls: $u = w = 0$ for $z = \pm 1$ and again the corresponding condition for pressure correction is $\partial\phi/\partial z = 0$.

So, the computations are carried out for several Reynolds numbers ranging from $Re = 50$ to 500. In each case, the mesh is refined close to the inlet section and near the walls, using the same kind of variable change as in the previous test case (see Appendix C). Table I summarizes the different cases, specifying in particular the mesh size and location of recirculating bubbles. The definitions of reattachment lengths and separation lengths $x_{r_2}/h, x_{s_1}/h, x_{s_2}/h$ are given on Figure 8.

The reattachment lengths on the bottom wall are reported in Figure 9. Figure 10 displays the secondary separation and reattachment lengths on the top wall.

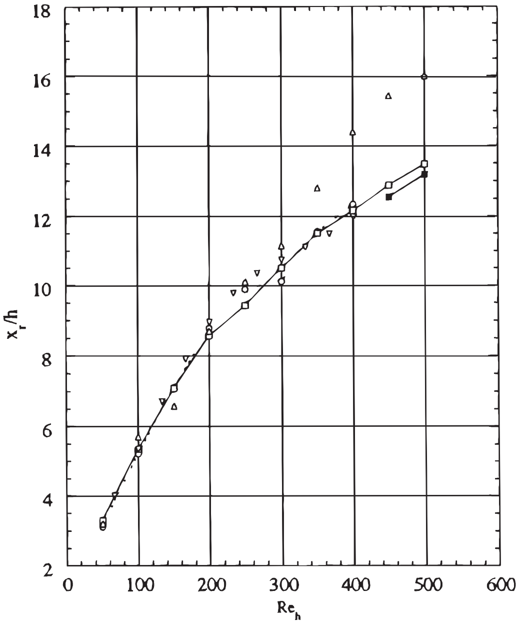

Figure 9. Main reattachment length versus Reynolds number in the laminar two-dimensional step flow in a channel. ○, centred differences, and zero gradient exit boundary condition; □, Hermitian schemes, and zero gradient exit boundary condition; ■, Hermitian schemes, and convective exit boundary condition; △, experiments, Armaly *et al.* (1983) [18]; ∇, numerical simulation, Le and Moin (1994) [19].

These results are compared to the experimental results of Armaly *et al.* [18] and to the numerical computations of Le and Moin [19]. A good agreement for the main reattachment length in Figure 9 is found up to $Re=250$ where some discrepancies appear between the numerical results and the experimental results. This is due to the development of three-dimensional effects in the experiments. The prediction of reattachment on the upper wall (Figure 10) is more subtle. Compared to the experiments, the fourth-order scheme shows improvement over the second-order scheme. Figure 11 displays some streamlines patterns for different Reynolds numbers (ranging from 100 to 500) together with the pressure levels. Between $Re=150$ and 200, we clearly observe a second recirculation bubble that begins to grow on the upper wall, as reported in Armaly for $Re=150$.

Two other computations have been carried out (for $Re=450$ and 500), using different outflow boundary conditions. In these latter cases u and w are imposed using convective conditions

$$\frac{\partial u}{\partial t}=-u\frac{\partial u}{\partial x},\quad \frac{\partial w}{\partial t}=-u\frac{\partial w}{\partial x}$$

and

$$\frac{\partial p}{\partial x}=0 \quad \text{for the pressure correction}$$

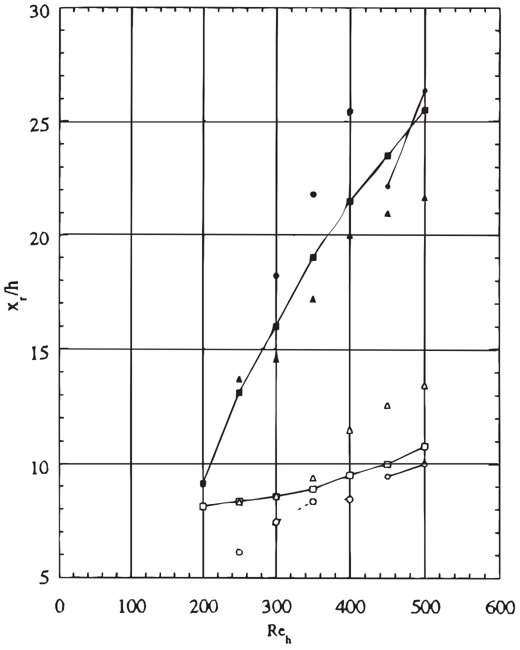

Figure 10. Reattachment length and separation at the upper wall versus Reynolds number in the laminar two-dimensional step flow in a channel. ○, x_{s1}/h for centred differences, zero gradient exit boundary conditions; ●, x_{s2}/h for centred differences, zero gradient exit boundary conditions; □, x_{s1}/h for Hermitian schemes, zero gradient exit boundary conditions; ■, x_{s2}/h for Hermitian schemes, zero gradient exit boundary conditions; ◇, x_{s1}/h for Hermitian schemes, convective exit boundary conditions; ◆, x_{s2}/h for Hermitian schemes, convective exit boundary conditions and △, ▲, experiment, Armaly *et al.* (1983) [18].

The results are reported in Figure 12 for $Re = 500$ in order to show that if the outlet section is located sufficiently far from the recirculating zone, then there is no practical difference.

4. LARGE EDDY SIMULATION OF TURBULENT RECIRCULATING FLOW

4.1. Filtered NS equations

Defining the filtered value $\bar{f}$ of a turbulent quantity f by

$$f(x', y', z') = \int f(x, y, z)\, G(x, y, z, x', y', z')\, \mathrm{d}x\, \mathrm{d}y\, \mathrm{d}z \tag{31}$$

The quantity G standing for a filter function depending on the mesh size, each flow variable can be split into an explicit grid scale contribution, the filtered quantity, and an implicit subgrid scale contribution. Thus, we write

$$\mathbf{U} = \bar{\mathbf{U}} + \mathbf{U}' \quad \text{and} \quad p = \bar{p} + p' \tag{32}$$

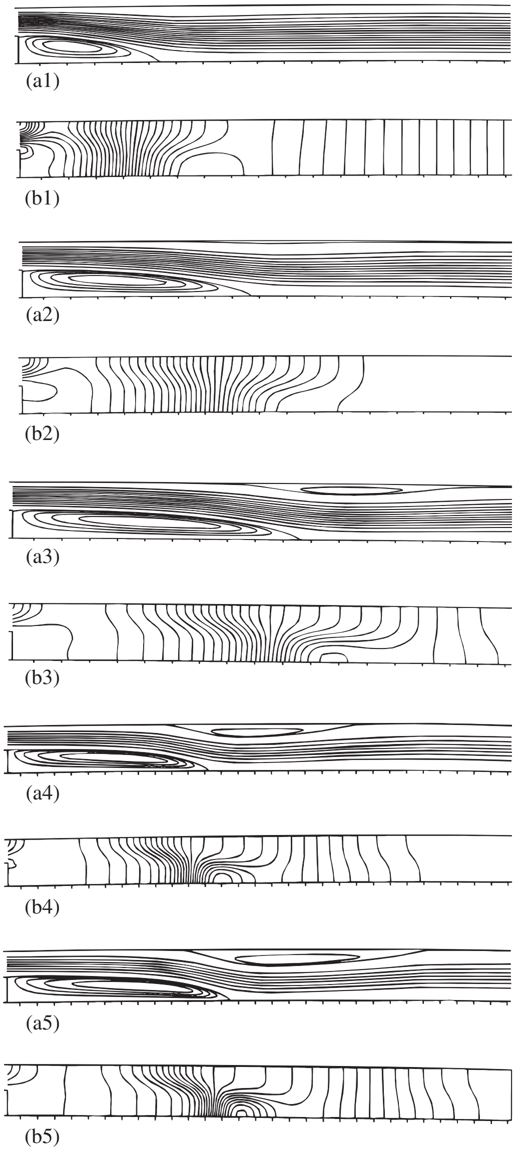

Figure 11. Streamlines and pressure contours in the laminar step flow in a channel, for several Reynolds numbers using zero derivative exit boundary conditions. (a) Streamlines and (b) isopressure contours. (1) $Re_h = 100$, (2) $Re_h = 200$, (3) $Re_h = 300$, (4) $Re_h = 400$, (5) $Re_h = 500$.

Applying this filtering operation to the NS equations, we get the so-called filtered Navier–Stokes equations (see e.g. Reference [20]):

$$\frac{\partial \bar{\mathbf{U}}}{\partial t} = -\frac{1}{2}[\bar{\mathbf{U}} \cdot \nabla \bar{\mathbf{U}} + \nabla(\bar{\mathbf{U}} \cdot \bar{\mathbf{U}})] - \nabla \bar{P} + \frac{1}{Re}\Delta \bar{\mathbf{U}} - \nabla \mathbf{T} - \nabla \mathbf{L} \tag{33}$$

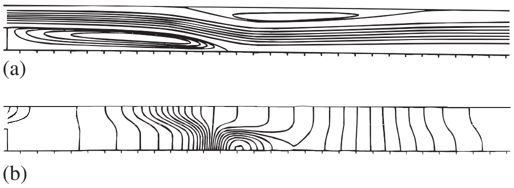

Figure 12. Streamlines and pressure contours in the laminar step flow in a channel, for Reynolds number 500 using convective exit boundary conditions.

along with the filtered continuity equation:

$$\nabla \cdot \bar{\mathbf{U}} = 0 \tag{34}$$

where $\mathbf{T} = \mathbf{R} - \frac{2}{3}k\mathbf{I}$ with $k = \mathrm{trace}(\mathbb{R})$ and $\mathbf{I} =$ unity tensor.

The tensor $\mathbf{T}$ is the deviatoric part of the subgrid scale Reynolds stress tensor defined by

$$\mathbf{R} = \overline{\mathbf{U}' \otimes \bar{\mathbf{U}}} + \overline{\bar{\mathbf{U}} \otimes \mathbf{U}'} + \overline{\mathbf{U}' \otimes \mathbf{U}'} \tag{35}$$

and $\bar{P}$ is the filtered modified pressure including the subgrid scale kinetic energy of turbulence:

$$\bar{P} = \frac{\bar{p}}{\rho} + \frac{2}{3}k \tag{36}$$

The cross terms in the $\mathbf{R}$ tensor contain both small-scale/small-scale interactions and small-scale/large-scale interactions. Since these terms are unknown, they have to be modelled.

The term $\mathbf{L}$ is the Leonard stress defined by:

$$\mathbf{L} = \overline{\bar{\mathbf{U}} \cdot \bar{\mathbf{U}}} - \bar{\mathbf{U}} \cdot \bar{\mathbf{U}} \tag{37}$$

Actually, a Gaussian filter is used in the spanwise direction whereas there is no explicit filtering operation in the two inhomogeneous directions (x and z), but the numerical scheme indeed implicitly filters in these directions.

4.2. Subgrid model

We use a Smagorinsky eddy viscosity model modified in the viscous sublayer in order to take into account the effect of Reynolds number like in Reference [21] which expresses the deviatoric stress tensor $\mathbf{T}$ with the local strain rate tensor $\mathbf{S}$:

$$\mathbf{T} = -2v_t\mathbf{S} \quad \text{with } \mathbf{S} = \tfrac{1}{2}(\nabla\bar{\mathbf{U}} + \nabla\bar{\mathbf{U}}^{\mathrm{T}}) \tag{38}$$

where v_t is the subgrid viscosity defined by

$$v_t = \begin{cases} v_{t_{\mathrm{outer}}} = (C_S l)^2(2S^2)^{1/2} & \text{for } d_{\mathrm{wall}} > d_p \\ v_{t_{\mathrm{inner}}} = C_2 \dfrac{l^4}{v}(2S^2) & \text{for } d_{\mathrm{wall}} < d_p \end{cases} \tag{39}$$

The term d_{wall} denotes to the distance from the nearest wall, d_p being the distance at which $\langle v_{t_{\mathrm{inner}}} \rangle_Y \geqslant \langle v_{t_{\mathrm{outer}}} \rangle_Y$.

The length scale, l, is given by

$$l = (\min(\Delta x, l')\min(\Delta z, l')\min(2\Delta y, l'))^{1/3} \tag{40}$$

with $l' = 0.1$ for $d_{\text{wall}} > 0.1$ and $l' = K d_{\text{wall}}$ for $d_{\text{wall}} < 0.1$ and C_s and C_2 are two constants given by $C_s = 0.2$ and $C_2 = C_S^2/27K$, K being the Von Karman constant $K = 0.41$.

More advanced models such as spectral-dynamic models [22] could be implemented in the numerical procedure.

The method is now applied to the case of the backward facing step flow in a channel or in a boundary layer in turbulent regime. These are typical test flows that are well documented in the scientific literature and representative of many usual situations encountered in real applications. The present aim is not a physical study of the flow structures. For this reason, the inlet channel flow upstream the step has not been considered in the calculation. The same practice has been followed in Reference [23] using a finite volume code with third-order accuracy. Indeed, considering that this flow is very sensitive to the inflow conditions, it would be necessary to incorporate the inlet channel flow (see Reference [24]) into the simulation in order to get a more detailed physical analysis of the flow.

The work of Neto *et al.* [23] on the step flow problem in a channel for a different Reynolds number than the one considered in the present work, is mainly devoted to physical and structural analysis using, among others, the structure function subgrid scale model. In the case of a step flow in a boundary layer, the DNS of Le *et al.* [29] gives detailed physical insight.

The present work focusses on numerical aspects and these test cases are used mainly to illustrate the capabilities of the numerical method. In this respect, let us emphasize that up to now, the diagonalization technique implemented in the present method, has seldom been used in LES calculations.

4.3. *Sudden expansion in plane channel flow*

We consider the turbulent flow in a channel with a sudden expansion (Figure 8).

Velocities are non-dimensioned with the maximum velocity U_m in the inflow section and the characteristic length scale is chosen to be the step height h. In this case, the size of the computational box is given by $L_x = 6\pi h$, $L_y = 3\pi h/2$ and $L_z = 2h$, and the Reynolds number is $Re = U_{\text{m}}h/\nu = 27\,600$.

A set of $48 \times 48 \times 62$ discretization grid points is used and the mesh is refined in the z-direction near the walls, in the centre of the channel at the step level and in the x-direction, near the inlet section (see Appendix C).

4.3.1. Boundary conditions. Owing to the turbulent nature of the flow, the boundary conditions have to be designed carefully, especially in the outflow section, to allow the flow and its convected eddies to go through.

At the walls, we use no-slip conditions for the three velocity components:

$$u_{i,N_z} = (-6u_{i,N_z-1} + u_{i,N_z-2})/3 \quad \text{and} \quad u_{i,1} = (-6u_{i,2} + u_{i,3})/3 \tag{41}$$

In spite of its simplicity and known limitations, model (39) can be used down to the wall allowing a complete calculation of the viscous sublayers using strong refinement of the mesh near the wall. This practice avoids the use of the logarithmic law of the wall which can be questionable [23].

At the inflow plane, the flow is assumed to be fully turbulent and each velocity component has to be specified at each time step. Thus, the data are provided by a previous turbulent channel flow simulation [1] for which the velocity components have been stored over 2000 time steps.

4.3.2. Frozen structures. Fixed pressure, along with $\partial v/\partial x = \partial w/\partial x = 0$ is not an appropriate exit boundary condition because the eddies are caused to collapse. The 'frozen turbulence' approximation produces an efficient solution of the problem. The turbulence signal is then split into a mean component (with respect to the spanwise direction) and a fluctuating component for each flow variable $f = \langle f\rangle + f^{\#}$. Two different types of conditions are used. For the mean part of velocities we use the following exit boundary conditions:

$\partial\langle w\rangle_Y/\partial x = \partial\langle v\rangle_Y/\partial x = 0$ and fixed pressure correction $\langle\Phi\rangle_Y = 0$ and the mean streamwise velocity component is extrapolated via the continuity condition:

$$\begin{aligned}(\langle u\rangle_Y)_{N_x-1+(1/2),k} = \Delta X\left[-23\frac{g_{z(k),k}}{g_{x(i),N_x-1}}\left(\frac{\partial\langle w\rangle_Y}{\partial Z}\right)_{N_x-1,k} + \left(\frac{\partial\langle u\rangle_Y}{\partial X}\right)_{N_x,k}\right]\\ + 26(\langle u\rangle_Y)_{N_x-2+(1/2),k} - (\langle u\rangle_Y)_{N_x-3+(1/2),k}\end{aligned} \tag{42}$$

The fluctuating part of velocities, denoted by the superscript (#), are given by the convective conditions:

$\partial\mathbf{U}^{\#}/\partial t + \mathbf{U}_{\mathrm{c}}\cdot\nabla\mathbf{U}^{\#} = 0$ with $\mathbf{U}_{\mathrm{c}} = (U_{\mathrm{c}}, 0, 0)$, U_{c} being a convection velocity. Actually, we take $\mathrm{U}_{\mathrm{c}} = (\langle u\rangle_Y)_{N_x-1,k}$. These relations give the explicit fluctuations:

$$\begin{aligned}u^{\#n+1}_{N_x-1+1/2,j,k} &= \frac{\Delta t U_{\mathrm{c}}}{\Delta x}\,u^{\#n}_{N_x-2+1/2,j,k} + \left[1 - \frac{\Delta t U_{\mathrm{c}}}{\Delta x}\right]u^{\#n}_{N_x-1+1/2,j,k}\\ v^{\#n+1}_{N_x,j,k} &= \frac{\Delta t U_{\mathrm{c}}}{\Delta x}\,v^{\#n}_{N_x-1,j,k} + \left[1 - \frac{\Delta t U_{\mathrm{c}}}{\Delta x}\right]v^{\#n}_{N_x,j,k}\\ w^{\#n+1}_{N_x,j,k} &= \frac{\Delta t U_{\mathrm{c}}}{\Delta x}\,w^{\#n}_{N_x-1,j,k} + \left[1 - \frac{\Delta t U_{\mathrm{c}}}{\Delta x}\right]w^{\#n}_{N_x,j,k}\end{aligned} \tag{43}$$

the corresponding condition for pressure correction is the homogeneous Neumann condition: $\partial\Phi^{\#}/\partial x = 0$.

Practically, the splitting is obviously realized by the Fourier transform in the y direction by distinguishing the zero k-mode (corresponding to $\langle f\rangle$) from the non-zero k-modes (corresponding to $f^{\#}$).

Another possible technique does not use splitting and assumes that the whole components are given by the convective relations:

$$\frac{\partial U}{\partial t} + U_{\mathrm{c}}.\nabla U = 0 \quad \text{with } U_{\mathrm{c}} = (U_{\mathrm{c}}, 0, 0) \tag{44}$$

The suitable condition for pressure correction is again an homogeneous Neumann condition in all the outflow plane. In this case, the streamwise component of velocity has to be renormalized with the given flow rate in order to fulfil the compatibility condition.

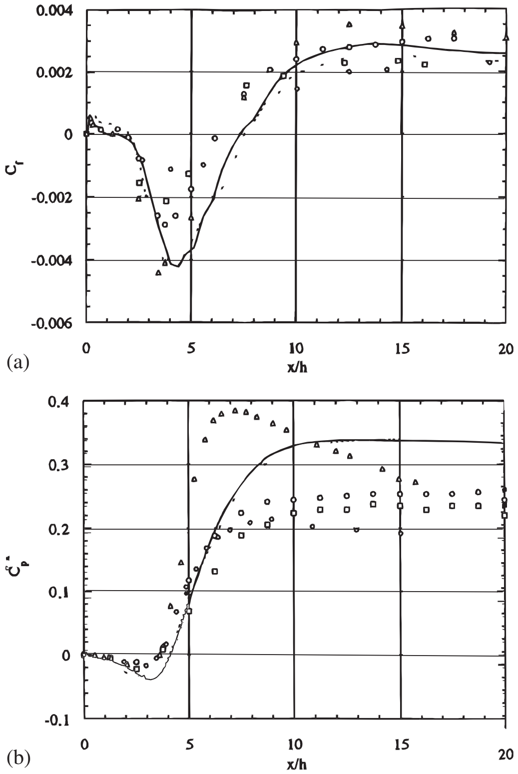

Figure 13. Friction factor and pressure coefficient at the lower wall in the backward facing step flow. (a) Friction factor: ——— Hermitian schemes; --------- centred second-order differences; ○: numerical predictions of Le and Moin (1994) [19]; □: Jovic experiment [28] ($Re_h = 10\,400$); ◇: Jovic experiment ($Re_h = 25\,500$); △: numerical predictions Le and Moin (1994), $Re_h = 500$, step in a channel. (b) Pressure coefficient: ——— Hermitian schemes; --------- centred second-order differences; ○: numerical predictions of Le and Moin (1994); □: Adams *et al.* [27] experiment, $Re_h = 26\,000$; ◇: Driver *et al.* (1985) [32] experiment, $Re_h = 36\,500$; △: Chandrsuda and Bradshaw [25] experiment, $Re_h = 100\,000$.

In the present case, these two types of exit boundary conditions give almost the same results.

4.3.3. Results. An important feature of the flow is given by the friction factor and by the pressure coefficient evolution along the wall. These are given in Figures 13 and 14 for the lower wall and the upper wall. A good agreement is found with various experimental and numerical data of the literature [25–28, 19]. Figure 15 shows the development of the Reynolds stress profiles downstream the step. The levels of energy are increasing in the mixing zone downstream the step angle and remain maximum before reattachment. After reattachment, the energy decreases and some local peaks appears near the walls relaxing toward a plane channel flow. Some minor differences are visible between the Hermitian solution and the centred difference solution.

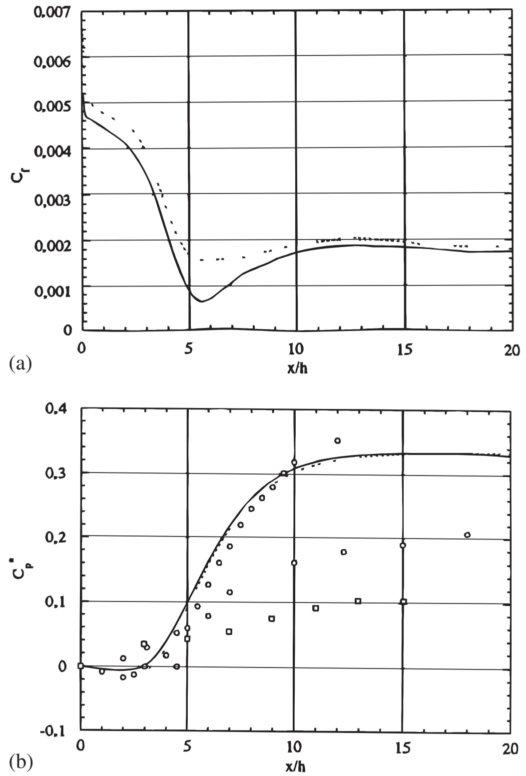

Figure 14. Friction factor and pressure coefficient at the upper wall in the backward facing step flow. (a) Friction factor: ———- Hermitian schemes; - - - - - - - - - centred second-order differences. (b) Pressure coefficient: ———- Hermitian schemes; - - - - - - - - - centred second-order differences; ○: numerical predictions of Le and Moin (1994) [19]; □: Driver *et al.* (1985) [32] experiment, $Re_h = 36\,500$; ■: Eaton *et al.* (1980) [27] experiment, $Re_h = 38\,000$.

4.4. Boundary layer over a backward facing step flow

We consider the turbulent flow in an open boundary layer with a small step height. In this case, the size of the computational box is given by $L_x = 20H, L_y = 3\pi H/2$ and $L_z = 5H$. Velocities are one-dimensioned with the maximum velocity U_{m} in the inflow section and length scales with the step height H. The Reynolds number is $Re_H = U_{\mathrm{m}}H/\nu = 13\,800$.

Two calculations have been carried out with a grid composed of $48 \times 48 \times 62$ discretization nodes using centred second-order differences (case A) or Hermitian schemes (case B). A third calculation (case C) based on Hermitian schemes uses a grid composed of $96 \times 64 \times 62$ discretization nodes. In all the cases, the mesh is refined near the walls, in the centre of the channel and near the inlet section.

4.4.1. Boundary conditions. In the inflow plane, the boundary conditions are obtained by the superposition of an analytical turbulent boundary layer mean profile (two dimensional) and a fluctuating field given by a previous simulation in a plane channel. These superimposed

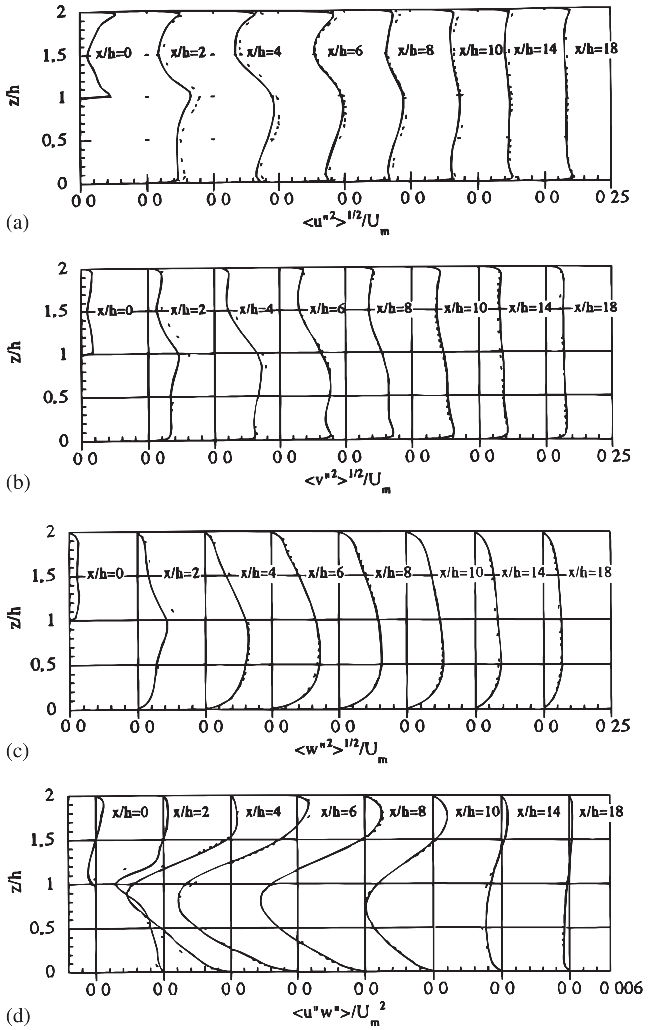

Figure 15. Turbulence intensities profiles and Reynolds shear stress profiles in the turbulent backward facing step flow. ——— Hermitian schemes; --------- centred second-order differences.

fluctuations are modulated by a sine function in order to get a zero level of turbulence at the external boundary. The boundary layer thickness is taken equal to the step height.

At the upper boundary, we use the following conditions:

$$\begin{aligned} &u_{i,N_z} = (-6u_{i,N_{z-1}} + u_{i,N_{z-2}} + 8U_{\text{ext}})/3 \quad \text{and} \quad u_{i,1} = (-6\mu_{i,2} + u_{i,3})/3 \\ &w_{i,N_z} = w_{i,N_{z-1}} \quad \text{and} \quad p = \text{constant} \end{aligned} \tag{45}$$

At the lower wall boundary and on the vertical wall, no-slip boundary conditions are used. For the outflow plane, the frozen structures boundary conditions are imposed.

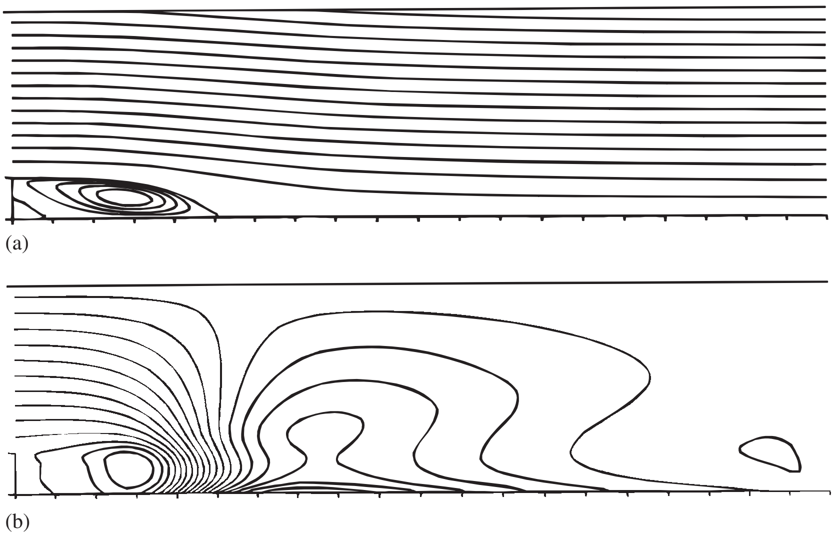

Figure 16. Streamlines and pressure contours in the turbulent backward facing step flow in a boundary layer for $Re_h = 13\,800$. (a) Streamlines and (b) pressure contours.

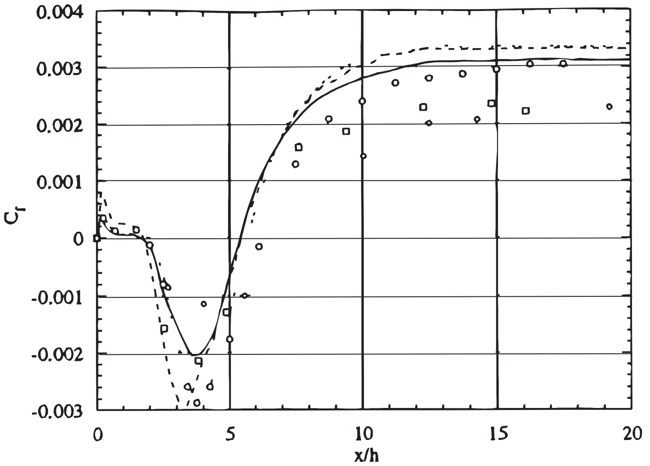

Figure 17. Friction factor at the wall in the turbulent backward facing step flow in a boundary layer. - - - - case A; --------- case B; ——— case C. ○, Numerical simulation Le and Moin (1994) [19]; □, Jovic experiment [28] ($Re_h = 10\,400$); ◇, Jovic experiment ($Re_h = 25\,500$).

4.4.2. Results. Streamlines and isopressure contours reported in Figure 16 exhibit the characteristic structure of the step flow. The important characteristic given by the evolution of friction factor along the wall is displayed in Figure 17 and compared to various experimental and numerical data. These curves allow to define the different zones of the flow: two recir-

Table II. Turbulent flow past a backward facing step in a boundary layer.

Case	x_{r1}/h	x_{r2}/h
A	1.76	5.45
B	1.92	5.64
C	1.70	5.40

culation zones exist, the first one which is very short, is located just down the step where C_f is positive, the second one is the main recirculation zone in which C_f is negative. In the next zone with again a positive friction factor, the boundary layer flow is recovering. These zones are defined in Table II. The values seem to be slightly below the experimental data and numerical data. Cases B and C give almost similar results but case C gives lower values that appears closer to [28] measurements, and thus probably more realistic. However, the case A gives a bad location for the minimum of friction factor. Discrepancies found further downstream, may probably be explained by Reynolds number effects. Besides, the relative low values of reattachment lengths can be due to a numerical effect found by Le *et al.* [19] who remarked that when the upstream section before the step is not calculated, the reattachment length is reduced. Figures 18 and 19 present the evolution of turbulent stress profiles downstream the step. The general behaviour of the turbulent field is found to be in agreement with the numerical simulation of Le *et al.* [29]. Cases B and C give similar results with turbulent levels that are somewhat lower than these found in case A. The difference between the results obtained using Hermitian schemes and the results obtained using the second order central differences is also visible in the case of the step in a channel. Indeed, the velocity variances are also affected by the effect of Reynolds number, but the u-component for instance clearly exhibits a major peak corresponding to the shear layer and a secondary peak very near the wall, probably linked to reverse flow where large eddies impinge the wall surface.

As an illustration, a low instantaneous isopressure surface is displayed on the perspective view of Figure 20, showing that the present numerical method can be used for insights into the structural details of the flow. However, the pressure field is not always a good marker of structures and it is doubtful that long spanwise quasi-bidimensional rolls correspond to the real shape of vortical eddies.

5. CONCLUDING REMARKS

The proposed method proved to give a practical and precise solution of the unsteady three-dimensional Navier–Stokes equations. This method that retains the flexibility of the finite differences schemes while giving high-order accuracy, usually a property of spectral methods, appears attractive to perform direct numerical simulations and large eddy simulations of turbulent flows. The original feature of the method is the use of an iterative solution of pressure–velocity coupling that preserves fourth-order accuracy on pressure while solving only a second-order pressure correction equation. The use of the skew-symmetric form is also an important ingredient that guaranties energy conservation properties, even on staggered grids. An important ingredient of the method is the diagonalization technique that presents decisive

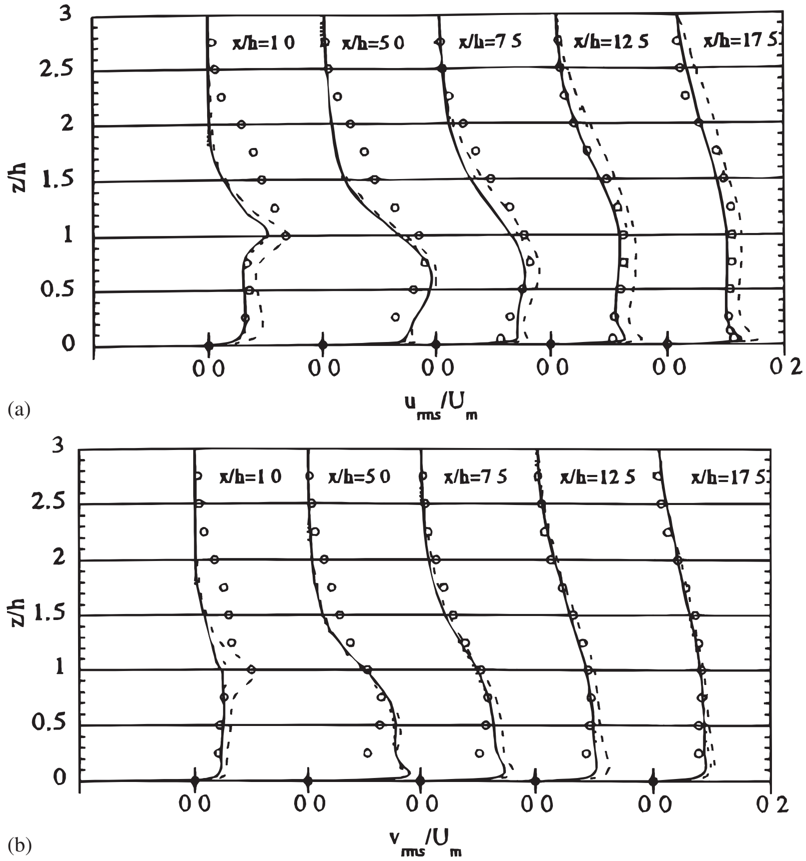

Figure 18. Turbulence intensities profiles in the turbulent backward facing step flow in a boundary layer. (a) Longitudinal component and (b) spanwise component _ _ _ _ , case A; _______, case B; ———, case C; ○, numerical simulation of Le and Moin (1994) [19].

advantages compared to usual iterative solutions. Indeed, the test applications to the turbulent flow after a backward facing step in a channel or in a boundary layer, produce a good description of the basic features of these flows compared to available data of the literature.

Considering the high accuracy permitted by the proposed method, combined with simplicity and effectiveness of the algorithm, it can be particularly useful for DNS or for instability growth applications [30]. These are the real potentials of the method. Useful applications of the method can be also related to laminar-turbulent transition for which high accuracy is essential. But indeed, in the case of LES of fully turbulent flows the advantages of fourth-order schemes over the second-order schemes appeared to be moderate. They are mainly noticeable on sensitive quantities such as the reattachment length for example, in the present application. Then, the second-order scheme would be generally sufficient for engineering applications (see Reference [31]).

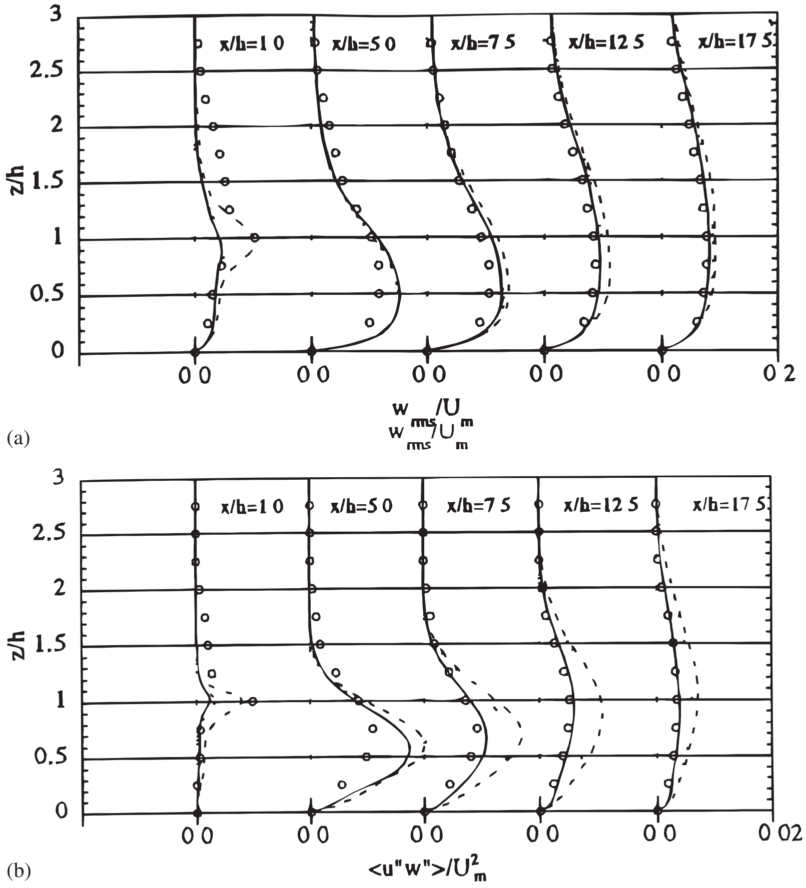

Figure 19. Turbulence intensities profiles and turbulent shear stress profiles in the turbulent backward facing step flow in a boundary layer. (a) Vertical component and (b) shear stress. _ _ _ _ , case A; _______, case B; ———, case C; ○, numerical simulation of Le and Moin (1994) [19].

APPENDIX A: DISCRETIZATION FORMULA

A.1. First-order Hermitian derivatives

The derivatives with respect to ξ (which denotes X or Z) of a function f defined at nodes $j-1, j, j+1$ are given on non-staggered grids by the following implicit relations [5]:

$$\Delta\xi\left(\left(\frac{\partial f}{\partial \xi}\right)_{j-1}+4\left(\frac{\partial f}{\partial \xi}\right)_{j}+\left(\frac{\partial f}{\partial \xi}\right)_{j+1}\right)=3(f_{j+1}-f_{j-1}) \qquad \text{(A1)}$$

at interior grid points.

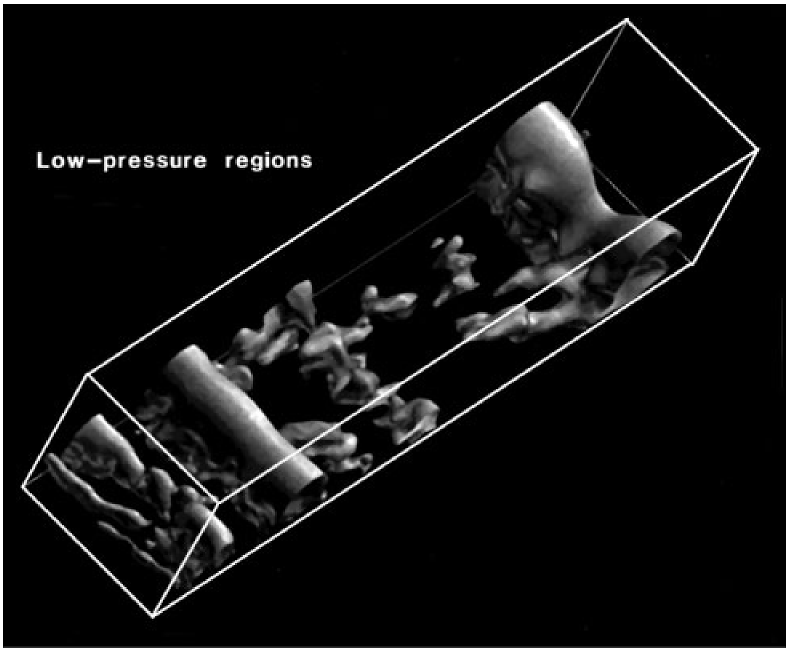

Figure 20. Isosurfaces at constant low pressure level $(p/\rho U_0^2 = -10^{-2})$ in a perspective instantaneous view.

At the boundaries we use the third-order accurate relations:

$$\begin{aligned}2\Delta\xi\left(2\left(\frac{\partial f}{\partial\xi}\right)_2+\left(\frac{\partial f}{\partial\xi}\right)_1\right)&=f_3+4f_2-5f_1\\ 2\Delta\xi\left(2\left(\frac{\partial f}{\partial\xi}\right)_{N-1}+\left(\frac{\partial f}{\partial\xi}\right)_N\right)&=-f_{N-2}-4f_{N-1}+5f_N\end{aligned}\tag{A2}$$

Since flow variables are located at different nodes, one requires to use first-order derivatives at staggered grid nodes as well as interpolation operators. These derivatives are provided by the implicit fourth-order accurate relations deduced from Taylor expansions:

$$\Delta\xi\left(\left(\frac{\partial f}{\partial\xi}\right)_{j-1}+22\left(\frac{\partial f}{\partial\xi}\right)_j+\left(\frac{\partial f}{\partial\xi}\right)_{j+1}\right)=24(f_{j+1/2}-f_{j-1+1/2})\tag{A3}$$

at interior grid points, and

$$\begin{aligned}\Delta\xi\left(23\left(\frac{\partial f}{\partial\xi}\right)_2+\left(\frac{\partial f}{\partial\xi}\right)_1\right)&=-f_{7/2}+26f_{5/2}-25f_{3/2}\\ \Delta f\left(23\left(\frac{\partial f}{\partial\xi}\right)_{N-1}+\left(\frac{\partial f}{\partial\xi}\right)_N\right)&=f_{N-3+1/2}-26f_{N-2+1/2}+25f_{N-1+1/2}\end{aligned}\tag{A4}$$

at the boundaries (third-order accuracy).

These equations lead to tridiagonal systems which are solved using the Thomas algorithm.

The relations for barycentric interpolation which are also fourth-order accurate are given by

$$f_{j+1/2} = (9f_{j-1} + 9f_j - f_{j+1} - f_{j+2})/16 \tag{A5}$$

and the third-order boundary relations:

$$\begin{aligned} f_{3/2} &= (6f_1 + 12f_2 - 2f_3)/16 \\ f_{N-1+1/2} &= (6f_{N-1} + 12f_{N-2} - 2f_{N-3})/16 \end{aligned} \tag{A6}$$

at the boundaries.

A.2. Second-order Hermitian derivatives

Second-order derivatives, evaluated on non-staggered grid nodes, are given by

$$\frac{\partial^2 f}{\partial \xi^2} = \delta^2_{\xi\xi} + \gamma_\xi\left(f, \frac{\partial f}{\partial \xi}\right) \quad \text{where } \gamma_\xi\left(f, \frac{\partial f}{\partial \xi}\right) = -\delta_\xi\left(\frac{\partial f}{\partial \xi}\right) + \delta^2_{\xi\xi} f \tag{A7}$$

The symbols δ_ξ and $\delta^2_{\xi\xi}$ represent the classical centred difference operators:

$$(\delta_\xi f)_j = \frac{f_{j+1} - f_{j-1}}{2\Delta\xi} \quad \text{and} \quad (\delta^2_{\xi\xi} f)_j = \frac{f_{j-1} - 2f_j + f_{j+1}}{(\Delta\xi)^2} \tag{A8}$$

A.3. Discretization of convective terms

Convective terms like $u\partial u/\partial x$ in the u momentum equation will be computed by an interpolation on non-staggered nodes (i, j, k), followed by a derivative on staggered nodes $(i+1/2, j, k)$:

$$\left(u\frac{\partial u}{\partial x}\right)_{i+1/2,j,k} = u_{i+1/2,j,k}\left(\frac{\partial u_{i,j,k}}{\partial x}\right)_{i+1/2,j,k} \tag{A9}$$

APPENDIX B: MODIFICATIONS IN THE DISCRETIZATION OF THE POISSON EQUATION

Condition (21) has to be preserved exactly by the numerical scheme:

$$\sum_{i,j,k}^{N_x-1,N_y,N_z-1} \frac{1}{\Delta t}(D.U)_{i,j,k} = \sum_{i,j,k}^{N_x-1,N_y,N_z-1} (\delta^2\Phi)_{i,j,k} \tag{B1}$$

Using $\Phi_{1,k} = \Phi_{2,k}, \Phi_{Nx,k} = \Phi_{Nx-1,k}$ and $\Phi_{i,1} = \Phi_{i,2}, \Phi_{i,Nz} = \Phi_{i,Nz-1}$ as approximations of (22), the right-hand side of Equation (22) cancels. With the periodicity assumption in the spanwise direction, the problem is then to ensure:

$$\sum_{j,k}^{N_y,N_z-1}\left(\sum_{i}^{N_x-1}\left(\frac{\partial u}{\partial x}\right)_i\right)_{j,k} + \sum_{i,j}^{N_y,N_x-1}\left(\sum_{k}^{N_z-1}\left(\frac{\partial w}{\partial z}\right)_k\right)_{i,j} = 0$$

Such is not exactly the case with the Hermitian relations (Appendix A) and the solution for this problem is to use the weighting coefficients α_i and β_k, as follows:

$$\sum_{i}^{N_x-1} \alpha_i \left(\sum_{j,k}^{N_y,N_z-1} \left(\frac{\partial u}{\partial x}\right)_{j,k} \right) + \sum_{k}^{N_z-1} \beta_k \left(\sum_{i,j}^{N_y,N_x-1} \left(\frac{\partial w}{\partial z}\right)_{i,j} \right)_{i,j} = 0$$

With this new integration formula, the discrete laplacian operator has to be replaced by

$$(A_{xx} + A_{zz} + d_y^2) \quad \text{such that} (A_{xx} f)_i = \frac{1}{\alpha_i} (\delta^2_{xx} f)_i \text{ and } (A_{zz} f)_k = \frac{1}{\beta_k} (\delta^2_{zz} f)_k$$

to ensure that r.h.s. of Equation (22) still cancels identically.

From the first derivatives relations on staggered nodes, the coefficients α_i and β_k can be easily deduced:

$$\alpha_i = 1 \text{ for } i = 5, \ldots, Nx - 4 \quad \text{and} \quad \beta_k = 1 \text{ for } k = 5, \ldots, Nz - 4$$

$$\alpha_2 = \beta_2 = \alpha_{N_x-1} = \beta_{N_z-1} = 13/12, \alpha_3 = \beta_3 = \alpha_{N_x-2} = \beta_{N_z-2} = 7/8$$

and

$$\alpha_4 = \beta_4 = \alpha_{N_x-3} = \beta_{N_z-3} = 25/24 \tag{B2}$$

APPENDIX C: VARIABLE MESHES

Variables meshes are introduced through variable changes in the x and z directions in order to take into account the steep gradients near the wall and also near the inlet of the channel. In the z direction, a classical hyperbolic tangent is used:

$$z = \frac{1}{a_z} \tanh\ (z \arg\tanh\ (a_z)) \tag{C1}$$

The variable change in the x-direction is analogous and allows to tighten the mesh near the inlet:

$$x = L_x \frac{1}{a_x}\, th \left(\frac{X}{L_x} \arg th\ (a_x) \right) \tag{C2}$$

When the a-parameters are taken very small, a uniform grid distribution is recovered.

Then,

$$g_x = \frac{a_x}{\arg\tanh\ (a_x)} \operatorname{ch}^2 \left(\frac{X}{L_x} \arg\tanh\ (a_x) \right)$$

$$h_x = \frac{2a_x^2}{L_x \arg\tanh\ (a_x)} \operatorname{sh} \left(\frac{X}{L_x} \arg\tanh\ (a_x) \right) \operatorname{ch}^3 \left(\frac{X}{L_x} \arg\tanh\ (a_x) \right)$$

$$g_z = \frac{a_z}{\arg\tanh\ (a_z)}\, \mathrm{ch}^2(Z \arg\tanh\ (a_z))$$

$$h_z = \frac{2a_z^2}{\arg\tanh\ (a_z)}\, \mathrm{sh}(Z \arg\tanh\ (a_z))\, \mathrm{ch}^3(Z \arg\tanh\ (a_z))$$

In the case of the step flow the variable change is:

$$z = h\,\frac{\tanh(a_{zl}(Z - Z_l)) + \tanh(a_{zl}Z_l)}{\tanh(a_{zl}(\eta - Z_l)) + \tanh(a_{zl}Z_l)} \quad \text{for } 0 \leqslant Z \leqslant \eta$$

$$z = A_2 \tanh(a_{z2}(Z - Z_2)) + B_2 \quad \text{for } \eta \leqslant Z \leqslant L_z$$

$$x = \frac{L_x}{a_x} \tanh\left(\arg\tanh(a_x)\,\frac{X}{L_x}\right)$$

For the present application, we have used for the step in a channel in the laminar case:

$$Z_1 = Z_2 = \eta, \quad a_{z1} = a_{z2} = 2.82 \quad \text{and} \quad a_x = 0.93$$

whereas A_2 and B_2 are chosen in order to enforce continuity in z and its first derivatives at η.

For the step in a channel in the turbulent case:

$$Z_1 = 0.675, \quad Z_2 = 2\eta - Z_1, \quad \eta = 1$$

For the turbulent step flow in a boundary layer:

$$\eta = 2, \quad Z_1 = 1.25, \quad Z_2 = L_{z1}, \quad a_{z1} = 1.5, \quad a_{z2} = 0.574$$

APPENDIX D: FOURIER PSEUDO-SPECTRAL TREATMENT IN THE SPANWISE DIRECTION

Derivatives and interpolations in the spanwise direction are based on Fourier expansions. The mesh is still staggered, using normal nodes for pressure and shifted grids for velocity:

$$y_j = j\Delta Y = jL_y/N_y \tag{D1}$$

$$y_{j+1/2} = (j + 1/2)\Delta Y = jL_y/N_y \tag{D2}$$

for $j = 0, 1, \ldots, N_y$.

The wavenumbers are defined by

$$k_j = j\Delta k_y = 2\pi j/L_y \tag{D3}$$

The couple of direct and inverse discrete Fourier transform are chosen in the following form:

$$\begin{aligned}\hat{f}(k_p) &= \frac{1}{N_y}\sum_{j=0}^{N_y-1} f(x_j)\exp(-ik_p x_j)\\ f(x_j) &= \sum_{p=-N_y/2}^{N_y/2-1}\hat{f}(k_p)\exp(ik_p x_j)\end{aligned} \tag{D4}$$

Thus, derivatives on normal and shifted nodes are given by

$$\frac{\partial f}{\partial y}(y_j) = \sum_{p=-N_y/2}^{N_y/2-1} ik_p\hat{f}(k_p)\exp(ik_p y_j)$$

and

$$\frac{\partial f}{\partial y}\left(y_j + \frac{\Delta y}{2}\right) = \sum_{p=-N_y/2}^{N_y/2-1} ik_p\hat{f}(k_p)\exp\left[ik_p\left(y_j + \frac{\Delta y}{2}\right)\right] \tag{D5}$$

with similar relations for second-order derivatives and for interpolations.

Also, noting the incomplete information on the $N_y/2+1$ Fourier mode, it will be forced to zero in the calculations:

$$\hat{f}(N_y/2+1) = 0 \tag{D6}$$

ACKNOWLEDGEMENTS

The computations have been carried out on C98 computers of the IDRIS in Paris who is gratefully acknowledged.

The authors acknowledge Dr. Pulicani (Univ. Aix-Marseille III) for the useful discussions they had on numerical techniques.

REFERENCES

1. Schiestel R, Viazzo S. A Hermitian–Fourier numerical method for solving the incompressible Navier–Stokes equations. *International Journal of Computers and Fluids* 1995; **24**(6):739–752.
2. Krause E. Mehrstellenverfahren zur Integration der Grenzschichtgleichungen. *DLR Mitteilung* 1971; **71**:109–119.
3. Hirsh RS. Higher order accurate difference solution of fluid mechanics problems by a compact differencing technique. *Journal of Computational Physics* 1975; **19**:90–109.
4. Peyret R, Taylor TD. *Computational Methods for Fluid Flow*. Springer: Berlin, 1983.
5. Elsaesser E, Peyret R. Méthodes hermitiennes pour la résolution numérique des équations de Navier–Stokes. In *Méthodes Numériques dans les Sciences de l'Ingénieur*, Absi E, Glowinsky R (eds). Dunod: Paris, (1979); 249–258.
6. Aubert X-L, Deville M. Steady viscous flows by compact differences in boundary fitted coordinates. *Journal of Computational Physics* 1983; **49**:490–522.
7. Bontoux P. Contribution à l'étude des écoulements visqueux en milieu confiné. Analyse et optimisation des méthodes numériques de haute précision. *Thèse Doct. Es Sc. Math.*, Univ. D'Aix-Marseille II, 1978.
8. Lele SK. Compact Finite difference schemes with spectral like resolution. *Journal of Computational Physics* 1992; **103**:16–42.
9. Kral LD, Zang TA. Large eddy simulation of supersonic, wall-bounded, turbulent flows. In *Instability*, *Transition and Turbulence*, Hussaini MY *et al.* (eds). Springer: Berlin. 1992; 589–599.
10. Guo Y, Adams NA. Numerical investigation of supersonic turbulent boundary layers with high wall temperature. In *Proceedings of the 1994 Summer Program Studying Turbulence using Numerical simulation Databases V*, Center of Turbulence Research, NASA Ames Res. Center and Stanford University CA, USA, 1994; 245–267.

11. Zang TA. Spectral methods for simulation of transition and turbulence. In *Spectral and Higher Order Methods for Partial Differential Equations. Proceedings of the ICOSAHOM89 Conference*, Como, Italy, 1989. Canuto C, Quarteroni A (eds). North-Holland: Amsterdam, 1990; 209–221.
12. Viazzo S. Simulations numériques de grandes structures turbulentes en canal plan appliquées à l'étude du champ de pression pariétal. *Thèse de Doctorat*, Université d'Aix-Marseille II, 1993.
13. Aubert X-L. Transformation de coordonnées et schémas compacts aux différences finies appliquées à la résolution des équations de Navier–Stokes. *Thèse de doctorat en Sciences Appliquées*, Louvain-la-Neuve, 1983.
14. Haidvogel D, Zang T. The accurate solution of Poisson's equations by expansion in Chebyshev polynomials. *Journal of Computational Physics* 1979; **30**:167–180.
15. Ehrenstein U, Peyret R. A Chebyshev collocation method for the Navier–Stokes equations with application to double diffusive convection. *International Journal for Numerical Methods in Fluids* 1989; **9**:427–452.
16. Védy E. Développement de simulations de grandes échelles turbulentes en présence de parois et application au champ de pression pariétal. *Thèse de Doctorat*, Université d'Aix-Marseille II, 1998.
17. Courant R, Hilbert D. *Methods of Mathematical Physics*. Interscience: New York, 1966.
18. Armaly BF, Durst F, Pereira JCF, Shonung B. Experimental and theoretical investigation of backward-facing step flow. *Journal of Fluid Mechanics* 1983; **127**:473–496.
19. Le H, Moin P. Direct numerical simulation of turbulent flow over a backward-facing step. *Report TF*-58, Department of Mechanical Engineering, Stanford University California, USA, 1994.
20. Schiestel R. Les écoulements turbulents: modélisation et simulation. Hermès: Paris (2nd edn), 1998.
21. Moin P, Reynolds WC, Ferziger JH. Large eddy simulation of incompressible turbulent channel flow. *Report TF*-12, Department of Mechanical Engineering. Stanford University, California, USA, 1978.
22. Lamballais E, Lesieur M, Silvestrini JH. Spectral-dynamic model for LES of free and wall shear flows. *11th Symposium on Turbulent Shear Flows*, Grenoble, France, Sept 8–10, 1997, *Proceedings* 28/7–28/12, 1997.
23. Silveira Neto A, Grand D, Métais O, Lesieur M. A numerical investigation of the coherent vortices in turbulence behind a backward facing step. *Journal of Fluid Mechanics* 1993; **256**:1–25.
24. Lesieur M. Recent approaches in large-eddy simulations of turbulence. In: *New Tools in Turbulence Modelling*, Les Houches School, May 21–31, 1996, Métais O, Ferziger J (eds). Springer, Les Éditions de Physique: Heidelberg, 1997.
25. Chandrsuda C, Bradshaw P. Turbulence structure of a reattaching mixing layer. *Journal of Fluid Mechanics* 1981; **110**:171–194.
26. Eaton J, Johnston J. A review of research on subsonic turbulent flow reattachment. *AIAA Journal* 1981; **19**(9):1093–110.
27. Adams E, Johnston J, Eaton J. Experiments on the structure of turbulent reattachment flow. *Report MD*-43, Department of Mechanical Engineering, Stanford University California, USA, 1984.
28. Jovic S, Driver D. Reynolds number effect on the skin friction in separated flows behind a backward facing step. *Journal of the Experimental Fluids* 1995; **23**:464–467.
29. Le H, Moin P, Kim J. Direct numerical simulation of turbulent flow over a backward-facing step. *Journal of Fluid Mechanics* 1997; **330**:349–374.
30. Viazzo S, Schiestel R. Simulation des grandes échelles turbulentes en canal à l'aide d'un schéma hermitien'. *Comptes Rendus des Seances del 'Academie des Sciences Paris Série IIb*. 1995; **321**:225–232.
31. Moinat P. Application des techniques de simulation des grandes échelles à un écoulement en géométrie complexe: la marche en dérapage. *Ph. D. Thesis*, Inst. Nat. Polytech. Grenoble, 1994.
32. Driver DM, Seegmiller HL. Features of a reattaching turbulent shear layer in a divergent channel flow. *AIAA Journal* 1985; **23**(2):163–171.